Tracing olivine carbonation and serpentinization in CO_2-rich fluids via magnesium exchange and isotopic fractionation

Jan Přikryl*[1], Andri Stefánsson[1] and Christopher R. Pearce[2]

[1] Institute of Earth Sciences, University of Iceland, Sturlugata 7, 101 Reykjavík, Iceland

[2] National Oceanography Centre Southampton, University of Southampton Waterfront Campus, European Way, Southampton, SO14 3ZH, UK

* Corresponding author: e-mail: jap5@hi.is

Abstract

Chemical exchange between seawater and the oceanic crust is thought to play a significant role in the regulation of the global magnesium (Mg) cycle, yet relatively little is known about the rates and mechanisms of Mg exchange in these crustal environments. In this study we experimentally characterize the extent, and nature, of Mg isotope fractionation during the carbonation and serpentinization of olivine (one of the principal minerals found in ultramafic rocks) under hydrothermal conditions. Olivine alteration was found to be incongruent, with the reactant fluid composition varying according to the extent of olivine dissolution and the precipitation of secondary minerals. In mildly acid water (pH ~6.5), olivine dissolved to form Mg-Fe carbonate solid solutions and minor chrysotile. Upon carbonation and a decrease of CO_2 in the water, the pH increased to >8, with chrysotile and brucite becoming the dominant alteration minerals. The Mg-rich carbonates preferentially incorporated lighter Mg isotopes, resulting in a ~0.5‰ increase of the δ^{26}Mg composition of the fluid relative to olivine during the initial carbonation and serpentinization reactions. This was followed by a decrease in δ^{26}Mg under higher pH conditions associated with the formation of brucite. Our experimental and modeling results therefore demonstrate that the δ^{26}Mg composition of fluids involved in olivine alteration reflect the type and quantity of secondary Mg minerals formed, which in turn depend on the pH and CO_2 concentration of the water. Comparison of these results with natural groundwaters and geothermal waters from basaltic terrains indicate that the δ^{26}Mg composition of natural waters are likely to also be controlled by mafic rock dissolution and the preferential incorporation of isotopically light Mg into carbonates and isotopically heavy Mg into Mg-Si minerals. Together, these findings improve our understanding of Mg isotope systematics during water-rock interaction, and suggest that δ^{26}Mg may be a useful tool for tracing reactions that are critical to geological CO_2 sequestration.

1. Introduction

Earth's hydrosphere, continental crust and oceanic crust contain <0.1% of the total Mg in the bulk Earth yet show the largest extent of Mg isotopic variation (e.g. Galy et al., 2003; Huang, 2013; Teng, 2017). Characterising the mechanisms and processes that control Mg isotopic fractionation and the isotopic balance of the bulk Earth can therefore improve our understanding of the global Mg cycle. The oceanic crust plays a significant role in global Mg budgets as it mainly consists of Mg-rich ultramafic and mafic rocks, with olivine one of the major primary minerals (e.g. McDonough and Sun, 1995). Furthermore, the alteration of olivine near and at the Earth's surface is fast relative to many other igneous minerals (e.g., Palandri and Kharaka, 2004) and involves the dissolution of olivine followed by precipitation of Mg-rich secondary minerals such as carbonates, chrysotile, talc and brucite (e.g., Janecky and Seyfried, 1986; Berndt et al., 1996). The serpentinization of mafic rocks also results in the generation of H_2 by water reduction through oxidation of ferrous iron (Fe^{II}) dissolved from the primary rocks like olivine. The H_2 formed may further lead to formation of inorganic hydrocarbons from reduction of inorganic carbon like CO_2 (e.g., McCollom and Seewald, 2001; Etiope and Sherwood Lollar, 2013). These reactions within mafic and ultramafic rocks have received growing interest from the scientific community as they represent a potential method for reducing atmospheric CO_2 concentrations by long-term CO_2 storage, as such rock types are a primary source of the principal cations (Mg^{2+}, Fe^{2+} and Ca^{2+}) needed for carbonate formation (e.g., McGrail et al., 2006; Gíslason et al., 2010; Matter et al., 2016).

Previous studies on the carbonation and serpentinization of mafic and ultramafic rocks have focused on characterizing water-rock interaction with seawater and meteoric

60 water under various pressures and temperatures (e.g., James et al., 2003; Giammar et al.,
61 2005; Béarat et al., 2006; Seyfried et al., 2007; Andreani et al., 2009; McCollom and Bach,
62 2009; King et al., 2010; Jones et al., 2010; Stefánsson, 2010; Daval et al., 2011; Hövelmann
63 et al., 2011; Gysi and Stefánsson, 2011, 2012a; Klein and Garrido, 2011; Marcaillou et al.,
64 2011; Marieni et al. 2013; Lafay et al., 2012; Neubeck et al., 2014). Alteration under these
65 conditions has been observed to result in the formation of various carbonate minerals at
66 elevated CO_2 concentrations and pH <7, whereas at low CO_2 concentrations the fluid pH
67 becomes more alkaline, resulting in the formation of clays and serpentine minerals.
68 Unfortunately, attempts to quantify the rate of carbonation and serpentinization within these
69 reactions (and hence the processes that influence them) is complicated by the fact that many
70 of the alteration minerals contain the same major elements as the primary phases. This means
71 that, in the absence of mineralogical evidence, any changes observed in Mg concentrations
72 can only be used to speculate on the extent of Mg-carbonate or silicate minerals being
73 precipitated. In contrast, the extent of isotopic fractionation varies between mineral phases
74 and reaction pathways, thus quantifying variations in the Mg isotope (δ^{26}Mg) composition of
75 the reacting fluids may help quantify the extent of carbonation and CO_2 mineral sequestration
76 associated with the alteration of mafic and ultramafic rocks.

77 Ultramafic and mafic oceanic rocks and mantle xenoliths show a relatively small
78 δ^{26}Mg range of -0.35 to -0.18‰ (e.g., Wiechert and Halliday, 2007; Teng et al., 2007, 2010,
79 2015; Liu et al., 2017). In contrast, continental basalts display more negative δ^{26}Mg values
80 of -0.60 to -0.35‰ as a result of incongruent partial melting of an isotopically light
81 carbonated mantle (e.g., Huang et al., 2015), while altered oceanic basalts show significant
82 δ^{26}Mg variations ranging from -2.76 to +0.21‰, suggesting significant Mg isotope
83 fractionation upon water-rock interaction (Huang, 2013). The lowest δ^{26}Mg ratios in these
84 altered basalts are typically associated with carbonation reactions, while the higher values are

generally associated with serpenitinization reactions. The fluids associated with these alteration reactions also have varying δ^{26}Mg compositions, with seawater having a uniform composition of -0.83±0.09‰ (e.g. Ling et al. 2011), while thermal and non-thermal groundwaters range between -0.96 and +0.64‰ (Pogge von Strandmann et al. 2008). Carbonate minerals formed in the altered rocks are typically enriched in ^{24}Mg relative to original silicate phases (Beinlich et al., 2014; Wimpenny et al. 2014). The variations observed in fluid δ^{26}Mg may result from Mg isotope fractionation upon water-rock interaction with different fractionation factors for different secondary minerals (Wimpenny et al., 2014; Voigt et al., 2016; Liu et al., 2017). Once they have been properly quantified, such differences may be used to trace the degree of water-rock interaction, including the carbonation and serpenitization of mafic and ultramafic rocks.

In this study, we conducted reaction path experiments and geochemical and isotope modeling of olivine alteration in CO_2-rich hydrothermal fluids as a function of reaction time and CO_2 concentration. Our kinetic reaction path model was prioritized to a mass balance approach in order to include a time dimension that enables us to extrapolate the geochemical reaction networks during reaction progress to natural systems. The reaction process was traced through time by solution chemistry, alteration mineralogy and Mg isotope systematics in order to define the major factors controlling water-olivine (mafic rock) alteration. Particular focus was placed on characterising the extent of δ^{26}Mg fractionation during the formation of secondary phases, and its potential for use as a mechanism of tracing CO_2 sequestration in mafic and ultramafic rocks.

2. Experimental methods

2.1. Material and experimental design

The olivine used in the experiments was collected from Almklovdalen peridotite massif, Western Gneiss Region, Norway (Brueckner et al., 2010). The source dunite samples contained over 90% olivine, which was handpicked, crushed in a jaw crusher and agate mortar and pestle then dry sieved. The 45-125 μm size fraction was used in all of the experiments. The grains were unzoned, and have a composition determined by EMPA (n = 23) of $Mg_{1.81\text{-}1.88}Fe_{0.13\text{-}0.15}Si_{0.97\text{-}1.01}O_4$. The sum of other elements was ≤0.36 wt%. Hereafter, the olivine composition is referred to as 93% forsterite (Fo_{93}). Prior to the experiments it was cleaned using deionized water, acetone and a magnet to separate any magnetic particles present, followed by drying at 40°C. The specific geometric surface area (A_{geo}) was determined according to the method of Tester et al. (1994) to be 226.3 cm^2/g.

The batch (closed-system) experiments of olivine alteration in CO_2-rich aqueous solutions were carried out at 5-21 mmol/kg initial total dissolved inorganic carbon (ΣCO_2) in a Parr stirring reactor made of titanium (Fig. 1). Prior to each experiment the 600 ml reactor was filled with ~53 g Fo_{93} and ~400 g of degassed CO_2-rich fluid under N_2 atmosphere, giving an initial fluid/rock ratio of ~8. The reactor was heated to 150°C with the pressure controlled by the solution vapor saturation pressure. The solutions were prepared from deionized water, NaCl (ACS, Sigma-Aldrich), $NaHCO_3$ (ACS, Sigma-Aldrich) and 37% HCl (pro. anal. Merck). The starting conditions of the experiments are summarized in Table 1.

2.2. Sampling and analysis

Solution samples were collected regularly throughout the experiments. Samples for pH determination were analyzed immediately using a combination pH electrode (Cole-Parmer) calibrated with commercial buffer solutions. Samples for CO_2 analyses were collected into 0.01-0.1 M NaOH solutions to prevent degassing and analyzed immediately using a modified

alkalinity titration (Stefánsson et al., 2007). Samples for Cl concentration determination were filtered through a 0.2 μm filter (cellulose acetate) followed by analysis using ion chromatography (Dionex-2000). Samples for Na, Mg, Si, Fe concentrations and Mg isotopic analyses were also filtered through a 0.2 μm filter, acidified to 1% HNO_3 (Merck Suprapur®) followed by analysis by ion chromatography for Na and Mg (Dionex-1000) and spectrophotometrically for Si and Fe (Dougan and Wilson, 1973; Fishman and Friedman, 1989). The analytical precision based on repeated analysis of an internal standard (GYG13) at the 95% confidence level was 4.4% for Na, 3.0% for Mg, 2.8% for Cl, 6.5% for Fe and 8.7% for Si.

Samples of the reacted solid were collected at the end of each experiment. These were dried at room temperature prior to analysis. The chemical composition of the material was determined using an electron microprobe (JEOL JXA-8200 Superprobe) with an accelerating voltage of 15 kV, a beam current of 15 nA, and a beam size of 5-1 μm. Unfortunately, most of the secondary phases (with the exception of magnesite) were too fine for point analysis, even with a beam size of 1 μm, and were too small to be visible on polished samples. The surface morphology of the olivine grains and secondary phases were also studied by scanning electron microscope (SEM) equipped with EDS (HITACHI TM-3000) at an accelerating voltage of 15 kV with a working distance of 6.8 mm. Finally, the samples were analyzed using powder x-ray diffraction (XRD) with scans collected for 9 hours with a Bruker D8 Advanced (CuKα1, 1.5406 Å; 2θ range 3-90; 0.01°/step and 768 s/step). Patterns were compared to standard mineral files compiled in the PDF2 database (ICDD PDF-2 Powder Diffraction File Database) using the software code EVA.

2.3. Magnesium isotope analyses

Solution samples were prepared for Mg isotopic (δ^{25}Mg and δ^{26}Mg) analysis by evaporating between 0.4 ml and 1.9 ml of solution in order to process ~2µg Mg per sample. Once dry each sample was dissolved in concentrated HNO_3, followed by drying and dissolution in 0.2 ml 0.8M HNO_3. For olivine, 5 mg of fresh sample was digested in HF-HNO_3 at 130 °C. Once dissolved the samples were dried down, dissolved in concentrated HCl, dried again, dissolved in concentrated HNO_3, dried down and then finally dissolved in 0.8M HNO_3. The solution and olivine samples were loaded onto acid-cleaned Teflon columns filled with a AG50W-X12 cation exchange resin to a height of 8.5 cm in 0.8M HNO_3. Magnesium separation followed the technique described by Pogge von Strandmann et al. (2011), with the sample being loaded and washed in 0.8M HNO_3 before the Mg fraction was eluted in 2M HNO_3. All samples were passed through the ion exchange columns twice to ensure complete separation from the other matrix elements, which was verified by ICP-MS analysis prior to isotopic analysis.

Isotopic analyses were performed on a ThermoFisher Scientific 'Neptune' Multi Collector Inductively Coupled Plasma Mass Spectrometer (MC-ICP-MS). Samples were introduced to the Ar Plasma in 2% aqueous HNO_3 using a standard sample induction system (SIS) attached to a PFA Teflon nebuliser. ^{24}Mg, ^{25}Mg, and ^{26}Mg were measured in low-resolution mode, with each analysis consisting of 1 block of 30 measurements per analysis. Solution concentrations of 600 ppb typically gave beam intensities of ~12 V for ^{24}Mg, with total procedural blanks having a negligible contribution of <12 mV. Isotopic compositions were determined via sample-standard bracketing, and are reported as δ^{26}Mg with respect to the DSM-3 standard (Galy et al., 2003). All sample analyses were run in duplicate, with the mean value and associated 2 standard error (se) reported (Table 4). Total procedural reproducibility was assessed by the analysis of the DSM, BCR, IAPSO and JDol standards

during the same measurement session, with the corresponding δ^{26}Mg values of +0.01±0.02‰, -0.26±0.10‰, -0.83±0.02‰ and -2.32±0.01‰ being identical to, or within error, of those previously reported by Pearce et al. (2012). The long-term reproducibility (2σ) of the δ^{26}Mg analytical protocol at the University of Southampton, determined by repeat analyses of the DSM-3 Mg standard, is 0.07‰.

The δ^{25}Mg and δ^{26}Mg systematics of the dataset show mass dependent behavior. It follows that δ^{25}Mg ratios do not provide additional information of magnesium isotope systematics beyond that of δ^{26}Mg, thus although the δ^{25}Mg data are reported in this study (Table 4) only the δ^{26}Mg results are used in the models and discussion.

3. Numerical simulations

3.1. Geochemical reaction path modeling

Reaction path simulations were carried out using the PHREEQC geochemical program (Parkhurst and Appelo, 2013). The Wateq.dat database used in these simulations was updated for dominant aqueous species, mineral solubilities and reaction kinetics of interest (Appendix 1).

The general rate expression used to simulate the progress of olivine dissolution, formation of secondary minerals and the associated solution chemistry was;

$$r_{\pm,T,i} = \pm \varsigma_i A_i \sum_i \left(k_{T,i} \prod_j a_j^x \right) (1 - \mathrm{SI}_i^n) \qquad (1)$$

where ς is the fraction of the surface area that is reactive having a value between 0 and 1 (Přikryl et al., 2017), A is the surface area, k_T is the rate constant at given temperature and

205 $\prod_j a_j^x$ is an activity expression for the *j*-th dissolved aqueous or surface species in solution.
206 The saturation index to the power of *n* standing for order of reaction, SI, is defined as;
207

$$SI = Q/K \quad (2)$$

208
209
210 where *Q* is the activity product of the mineral reaction and *K* is the respective equilibrium
211 solubility constant.
212 The surface area of the dissolved phase was expressed as decreasing upon dissolution
213 or loss of moles, assuming the grains to be spherical, i.e.
214

$$A = A^0 \left(\frac{m_t}{m_0}\right)^{2/3} \quad (3)$$

215
216 where m is number of moles. The secondary minerals were also allowed to dissolve with the
217 principle of microscopic reversibility. The rate expressions for secondary mineral formation
218 represent crystal growth rates of a given mineral surface. However, the initial formation of
219 minerals and mineral surfaces involves nucleation with $A = A_n$ whereas A_n is the total surface
220 area of the nuclei formed for a given mineral. In this study nucleation was not included into
221 the rate expression. Instead, the initial surface area of the secondary minerals was assigned
222 with A_n representing 0.1-10% of the initial olivine surface area. The surface area of growing
223 phases was 1% in the presented models. The purpose of varying the A_n value was to study the
224 effect of this initial surface area of secondary minerals on the model results. For the mineral
225 formation, the value of ς was taken to be 1.
226

3.2. Isotope modeling

The variations in δ^{26}Mg were simulated as a part of the reaction path model in a similar manner as described previously (e.g., Stefánsson and Barnes, 2016; Stefánsson et al., 2016; Stefánsson et al., 2017; Gunnarsson-Robin et al., 2017). In this context, the isotopic composition of the system (water-rock reaction in the reactor) can be defined as;

$$\delta^{26}Mg^{system} = \sum_{s} x_s \delta^{26} Mg_s = \sum_{i} x_i \delta^{26} Mg_i \quad (4)$$

where *s* denotes the various sources and their isotope values. As olivine is the only source of Mg in the system, the δ^{26}Mg composition of the system becomes equal to that of olivine ($\delta^{26}\mathrm{Mg}^{\mathrm{system}} = \delta^{26}\mathrm{Mg}_{\mathrm{olivine}}$). *i* denotes the i-th aqueous species and mineral being formed, and x_i is the mole fraction defined by:

$$x_i = \frac{n_i}{\sum_i n_i} \quad (5)$$

where *n* is the number of moles of Mg in the i-th aqueous species and/or minerals. Isotopic fractionation due to chemical reactions including the formation of secondary minerals can be calculated as a function of reaction progress (Ξ), where

$$n_i = n_i^o + \upsilon_i \Delta\Xi \quad (6)$$

where $n_i^o and\ \upsilon_i$ are the initial mole number and stoichiometry coefficient of the i-th aqueous species and minerals.

The isotope values of aqueous species and minerals is subsequently calculated from,

$$\delta^{26}Mg^{system} = x_k\delta^{26}Mg_k + \sum_i x_i\,(\alpha_{i-k}(1000 + \delta^{26}Mg_k) - 1000) \quad (7)$$

$$\delta^{26}Mg_i = \alpha_{i-k}(1000 + \delta^{26}Mg_k) - 1000 \quad (8)$$

where *k* is the key aqueous species or mineral, here taken to be Mg^{2+}. α_{i-j} is the equilibrium isotope fractionation factor between the *i*-th and *k*-th phases defined by;

$$\alpha_{i-k} = \frac{1000 + \alpha^{26}Mg_i}{1000 + \alpha^{26}Mg_k} \quad (9)$$

The values for the fractionation factors between Mg^{2+} and various secondary minerals, and their associated sources, are listed in Table 2 and shown in Fig. 2. The minerals included Mg-carbonates (magnesite and Mg-Fe carbonate solid solutions), talc, brucite and chrysotile (which was taken to be equivalent to that of chlorite). In order to obtain the fractionation factors under the experimental conditions of 150°C, the reported fractionation factors were fitted assuming a linear relationship between $10^3\ln\alpha$ and $1/T^2$ with a zero intercept at infinite temperature ($\alpha \rightarrow 1$ at $1/T^2 \rightarrow 0$) (Fig. 2), similar to Huang et al. (2013).

4. Results

4.1. Solution composition

Two types of experiments were conducted at 150°C: (1) low CO_2 concentrations of 5.17 - 6.36 mmol/kg (Experiments F, G and H), and (2) elevated CO_2 concentrations of 13.7 - 20.9

mmol/kg (Experiments K and E). The changes in solution chemistry as a function of reaction time are given in Table 3. Initially the pH of the solutions was ~6.5 and increased to between ~6.7 and ~7.5 with reaction time. The pH increased with decreasing aqueous CO_2 concentration. The dissolved concentrations of Si and Mg increased rapidly during the first hours, reaching values of Si ~0.4-1.2 and Mg ~0.7-1.1 mmol/kg after ~30 minutes followed by a decrease with experimental duration after ~1-10 days. An increase in Si concentration observed in experiment E from day 2 was significant compared to runs with lower CO_2 concentration. The high CO_2 experiments resulted in greater mass of dissolved olivine, and a corresponding faster intake of Mg ions by secondary phases from solution, relative to the low CO_2 experiments. Very low concentrations (generally less than ~1 μmol/kg) were also initially observed for Fe.

Variations in the δ^{26}Mg composition of the reacting fluid were determined together with the composition of the reacting olivine in experiment E, which showed the greatest change in Mg concentration (Table 4). The δ^{26}Mg ratio determined for the olivine sample was -0.22±0.07‰, and no variation between the initial and reacted material was observed. This is similar to the previously observed δ^{26}Mg ratio of unaltered oceanic crust and mantle xenolites of -0.35 to -0.18‰ (e.g., Wiechert and Halliday, 2007; Teng et al., 2007, 2010, 2015; Liu et al., 2017). The δ^{26}Mg ratios of the experimental solutions ranged from -0.27 to +0.35‰, was low initially, increased during the first five days followed by a relatively steady value.

4.2. Secondary mineralogy

The identified secondary minerals were magnesite, chrysotile/lizardite, amorphous silica and halite. Halite was considered to form upon quenching of the experimental systems. SEM images of the alteration products with altered olivine surfaces are shown in Figure 3. The

293 unaltered olivine surfaces showed pristine and smooth surfaces with sharp mineral edges.
294 Upon dissolution, conical or funnel-shaped etch pits were observed to form along the mineral
295 edges and within the previously smoothed surfaces. The composition of the
296 chrysotile/lizardite was determined to be $Mg_{2.87}Fe_{0.19}Si_{1.96}O_5(OH)_4$ and the composition of
297 magnesite was $Mg_{(0.92\text{-}0.95)}Fe_{(0.08\text{-}0.05)}CO_3$. No precipitating iron oxides were observed, Fe
298 released from the dissolving olivine was mostly incorporated into the magnesite and/or
299 chrysotile/lizardite solid solutions.

300 The changes in mineralogy as a function of reaction time at constant initial CO_2 (~6
301 mmol/kg; Experiments G and H) are shown in Figure 3 (d and e). Small single euhedral
302 crystals of magnesite formed up to 1 μm. Randomly distributed needle shaped formations, up
303 to 0.5 μm in length, are chrysotile/lizardite. No major dissolution features on the olivine
304 surfaces were observed after 7 days (Fig. 3d). After two weeks, no large changes were
305 observed except magnesite crystals grew and became larger, up to 3 μm in size. After 4
306 weeks of interaction (Fig. 3e), the formation of magnesite was characteristic with euhedral
307 crystals up to 5 μm in diameter. A thin layer of coarse alteration coating developed partly
308 over the olivine surfaces, typically as scales sticking out from the surface and no thicker than
309 0.5 μm; this is an early stage of chrysotile/lizardite nucleation and serpentinization.
310 Dissolution etch pits were also clearly observed on the olivine grain edges after four weeks of
311 interaction.

312 The effect of changing initial CO_2 concentration (Experiments H and E) on the olivine
313 alteration mineralogy is shown in Figure 3 (e and f). At low CO_2 (~6 mmol/kg; Exp. G, F, H;
314 Fig. 3d, e), magnesite crystals were observed to form along the olivine edges and within
315 conchoidal fractures whereas small chrysotile/lizardite needles formed randomly over the
316 whole olivine surface. However, for experiments with initially elevated CO_2 (~21 mmol/kg,
317 Exp. E; Fig. 3f), the magnesite crystals grew up to 10 μm in size with some of the olivine

grains completely coated with conglomerates of euhedral magnesite crystals after 25 days. Honeycomb structures or mesh texture of chrysotile/lizardite coated some of the olivine surface (Fig. 3f) and formed conglomerates around the magnesite crystals.

5. Discussion

5.1. Olivine alteration

The experimental results are compared with the calculated solution composition and mineralogy in Figures 4 and 5. The experimental solution composition was reasonably well reproduced by the geochemical models (Fig. 4). A declining trend for CO_2 concentration was observed in all experiments and models with time. Similarly pH values increased in both the experiments and models, reflecting the decreasing acid supply in the system. Some discrepancies were observed for Si (Fig. 4c), and are considered to be related to an initial non-stoichiometric dissolution of Si from the olivine and precipitation of silica coating (Pokrovsky and Schott, 2000; Daval et al., 2011; Saldi et al., 2013), supported by close to saturation values in the fluid samples. This could indicate the rapid formation of a SiO_2-rich coating (Saldi et al., 2015) and its subsequent breakdown after one day of reaction, which results in an increase of Si concentration. The experimental preferential release of Mg from olivine is probably masked by the incipient precipitation of magnesite from solution. For Mg, the modeled concentrations were lower than the experimental data until ~3 days of interaction. Afterwards a close match was observed between experiments and models. It is likely that the difference between model and experimental data reflects an initial overestimation of the extent of secondary mineral precipitation or not accounted SiO_2-coating, as the changes in CO_2 concentration showed good agreement between modeled and experimental system (Fig 4).

The secondary mineralogy predicted by the geochemical models shows a clear trend with reaction time and solution pH (Fig. 5); at pH<6.5, chrysotile and Mg-Fe carbonate solid solutions dominate the alteration mineralogy, but with increasing reaction time and pH brucite also becomes important. Brucite was not observed as a part of the alteration products in our experiments as the pH of the solutions was not high enough to initiate brucite formation (Pokrovsky and Schott, 2004; Li et al., 2014) at the end of the experiments. The amount of reacted initial CO_2 (Fig. 5a, b) is reflected by the amount of dissolved olivine mass and formed secondary minerals. The high CO_2 run dissolved ~6 times more olivine than the low CO_2 run (Fig. 5a, b), resulting in an order of magnitude difference in the amount of magnesite and talc that were precipitated. However, the relative proportion of the two minerals being formed was similar in both scenarios.

The results of the experiments and geochemical modeling demonstrate that the main factors controlling olivine-fluid interaction in CO_2-rich solutions are the extent of the reaction (Ξ) (or reaction time) and pH. Solution pH is in turn controlled by acid supply and the extent of reaction. For olivine alteration, where CO_2 is the major carbonic acid, two alteration stages were distinguished based on the changes in pH (Figs. 4 and 5): (1) stage **I** was characterized by mildly acid to neutral pH values, buffered by dissolved CO_2 and H^+ consumption upon olivine dissolution, and by the formation of Mg-Fe carbonate solid solutions and chrysotile; stage **II** (only reached through the geochemical modeling for the considered time-frames) was characterized by progressive olivine alteration, decrease of CO_2 concentration due to carbonate mineral formation, and an increase in pH to >8. Under these alkaline conditions chrysotile, brucite and Mg and Fe containing carbonates were formed. Similar pH effects on the alteration product have been observed during fluid-rock reactions with basaltic glasses (Gysi and Stefánsson, 2012a, 2012b).

The amount of secondary mineral formation was found to largely depend on the reactive surface area of the olivine (Fig. 5c). The best fit corresponded to 30% ($\varsigma = 0.3$) and 80% ($\varsigma = 0.8$) (Eqn. 1) coverage of the total olivine geometric surface under the low- and high CO_2 concentrations, respectively. This is in agreement with other studies (e.g. Brantley and Mellott, 2000; Lüttge and Arvidson, 2008), and implies only fraction of mineral surface is commonly reactive (although the potential influence of stirring rate and water-rock ratios within the reactors cannot be discounted). In contrast, the nucleation surface area (A_n) of secondary minerals was found to have a limited effect on the mass of secondary minerals formed. This observation is related to the fact that the secondary minerals reached close-to-equilibrium conditions with the fluid relatively quickly, thus their formation rates were primarily driven by the affinity term ($1\text{-}SI^m$), rather than the surface area of the nuclei and crystals (Pokrovsky and Schott, 2004).

The rate limiting reaction controlling elemental transfer is generally thought to be the dissolution rate of the primary mineral (e.g. Park and Fan, 2004; Hänchen et al., 2006). However, as pointed out by Saldi et al. (2012), this may not always be the case, as the precipitation rate of magnesite is 3-5 orders of magnitude lower than the corresponding dissolution rate for olivine. Here, we observed that olivine alteration rate primarily depends on pH. For example; the dissolution rate of olivine at a pH of ~6.5 was slightly greater than the formation rate of carbonates, demonstrating that the rate limiting factor of carbonation in the system was not the dissolution rate of olivine, but the precipitation rate of the carbonates. Similarly, with increasing reaction progression within the models the pH increased to >8 and under these conditions the dissolution rate of olivine became slower than the formation rates of all secondary minerals, implying that the rate limiting factors during water-rock interaction of olivine was its dissolution rate.

5.2. Magnesium isotope systematics during olivine carbonation and serpentinization

The only source of Mg in the experimental system was the olivine powder, which had a starting δ^{26}Mg ratio of -0.22±0.07‰ (Table 4). The initial alteration of the olivine in CO_2-rich water (stage **I**) was characterized by Mg dissolution from the olivine, buffering of the pH at ~6.5 and formation of Mg-Fe carbonates and chrysotile. Assuming equilibrium fractionation between the solution and the Mg-Fe carbonates (α = 0.99975) and chrysotile (α = 0.9988) at 150°C, the modeled olivine alteration resulted in the solution becoming enriched in ^{26}Mg and the alteration product enriched in ^{24}Mg (Fig. 6a). This is indeed what was observed experimentally, as upon initial dissolution the δ^{26}Mg ratio of the solution was similar to that of olivine (between -0.27 and -0.14‰), whereas the δ^{26}Mg composition of the solution increased to between +0.26 and +0.35‰ following the formation of Mg-Fe carbonates and chrysotile (Fig. 6b).

In the subsequent alteration stage of olivine (stage **II**) the modeled CO_2 concentration decreased due to carbonate mineralization and the solution pH increased to >8, with chrysotile and eventually brucite becoming the dominant alteration product. The equilibrium fractionation factors applied between the solution and brucite (α = 1.0004; Wimpenny et al., 2014; Li et al., 2014) and talc (α = 1.0004; Beinlich et al., 2014) resulted in the solution becoming enriched in ^{24}Mg and the alteration product enriched in ^{26}Mg, which is the reverse δ^{26}Mg systematics compared to the initial phase of olivine alteration.

These results suggest that changes in the δ^{26}Mg composition of the solution may be used to trace the extent of olivine alteration via carbonation and serpentinization reactions: Figure 6 demonstrates that the δ^{26}Mg composition can change rapidly (i.e. in a few days) under far from equilibrium to close to equilibrium conditions for both the carbonate minerals and the solution before stage **II** is reached. This is most likely caused by rapid element transfer during stage **I,** where the olivine dissolution and carbonation reactions predominantly

occur under far-from equilibrium conditions. This indicates that the dominant reaction pathway can be identified with δ^{26}Mg, thus the system could be used as a mechanism to verify ongoing carbonate formation within an ultramafic CO_2 sequestration system, as the extensive precipitation of Mg-carbonate minerals (presented in studied system as stage **I**) with light δ^{26}Mg composition will be reflected by the solution enriched in δ^{26}Mg. Of course, the accurate determination of the fractionation factors associated with the secondary phases being formed is crucial for application of isotopic modeling approaches such as that applied here. There is still a significant lack of understanding about how Mg isotopes are fractionated between different phases, and what the fractionation factors are for specific minerals, thus an in-depth review and assessment of the reported fractionation factors is required before using such techniques to quantify the extent of carbonation in natural settings.

5.3. Comparison with natural analogues

The results of our experiments and isotopic modeling are compared with naturally altered basalts, groundwaters and geothermal waters in Figure 7. The higher δ^{26}Mg values of the solutions measured in this study (relative to the starting olivine composition) are similar to the elevated values of +0.23 ‰ to +0.85 ‰ observed in the groundwaters and geothermal waters of the basaltic terrain in Iceland (Pogge von Strandmann et al., 2008). This positive shift in the δ^{26}Mg composition of the fluid is likely to be due to the formation of clay minerals (similar to serpentine minerals) and carbonate minerals that are enriched in ^{24}Mg relative to the olivine and bulk Mg of the basalts. Similarly, the δ^{26}Mg compositions of altered oceanic basalts in the western Pacific reveal large isotopic fractionation during oceanic crust alteration (Huang, 2013), with the most negative values being associated with the carbonation of the basalts, and less negative values associated with serpentinization. These observations are in good agreement with our isotopic modeling, where the carbonates

(and to a lesser extent chrysotile) are found to be enriched in the ^{24}Mg isotope relative to olivine and the solution, whereas extensive serpentinization of oceanic crust and formation of brucite and talc may result in the reversed $\delta^{26}Mg$, with these minerals becoming enriched in ^{24}Mg and the resulting solutions enriched in ^{26}Mg.

The hydrothermal carbonation of ultramafic rocks (and by analogy mafic rocks) is thought to be accompanied by significant inter-mineral fractionation resulting in the formation of ^{24}Mg enriched magnesite and ^{26}Mg enriched talc (Beinlich et al. 2014). The field results of Beinlich et al. (2014) suggest that Mg isotopes may not be fractionated during serpentinization reactions, as their olivine exhibits and invariant Mg isotope ratio. This study is in agreement that formation of Mg-bearing carbonates during ocean water circulation through mid-ocean ridge flanks at hydrothermal conditions forms a sink for isotopically light Mg. Our models show that the late stage serpentinization with limited Mg supply from slowly dissolving olivine and slowly forming chrysotile-brucite caused hydrothermal water to be progressively enriched in ^{24}Mg.

Together these analogues support our experiments and models and confirm the sensitivity of $\delta^{26}Mg$ to the formation and dissolution of different minerals under different settings. Quantifying the extent of reaction progress in natural systems can be complicated, however, as they contain multiple sources and sinks that can be isotopically heterogeneous (Teng, 2017), and the isotopic fractionation effects are not always preserved during the course of the reaction, and may be even absent if the precipitation of secondary phases occurs at close to equilibrium conditions (cf. Tang et al., 2008; Pearce et al., 2012; Mavromatis et al., 2017). Nevertheless, this study demonstrates that it can be possible to track these reactions in relatively simply Mg-rich systems by applying kinetic Mg isotope fractionation models for the rock-forming minerals that have been calibrated by laboratory experiments, theoretical calculation and the analysis of natural samples, and that under such settings the

467 δ^{26}Mg system could be used as a mechanism to test whether carbonate formation is ongoing
468 within an ultramafic CO_2 sequestration system.
469
470 **6. Conclusions**
471
472 Olivine carbonation and serpentinization in CO_2-rich fluids at 150˚C was studied
473 experimentally and by geochemical modeling. The alteration of olivine was found to be
474 dependent on reaction time, with two main stages being identified: Stage **I** was characterized
475 by a low pH (buffered at ~6.5), during which olivine dissolved to form Mg-Fe carbonate
476 solid solutions and minor chrysotile. Mg-rich carbonates and chrysotile forming during this
477 interval preferentially incorporated ^{24}Mg, such that the alteration product had lower δ^{26}Mg
478 values and the solution higher δ^{26}Mg relative to the olivine that provided the only source of
479 Mg in the experiments. Stage **II** continued the extensive alteration of olivine, with the
480 carbonation reactions ultimately driving a decrease of CO_2 concentration and associated
481 increase in pH (to >8), under which chrysotile and brucite became the dominant alteration
482 minerals. As a result, the alteration product became progressively enriched in ^{26}Mg relative to
483 the solution, such that the fluid may, given sufficient reaction time, display lower δ^{26}Mg
484 ratios than for the olivine source.
485 It follows that changes in the δ^{26}Mg composition of the fluid phase and alteration
486 products formed during olivine alteration directly reflect the type and quantity of secondary
487 Mg minerals formed, and thus in turn depend on pH and extent of reaction. Comparison of
488 the experimental and isotopic modeling results with groundwaters and geothermal waters of
489 basaltic terrains confirms that δ^{26}Mg systematics of the natural waters are controlled by mafic
490 rock dissolution and the incorporation of ^{24}Mg into carbonates and Mg-Si minerals such as
491 chrysotile and clays. The results also demonstrate that the extent of isotopic fractionation

driven by geochemical processes such as water-rock interaction may exceed the differences observed between the various sources, highlighting the effects and importance of such reactions on the isotope characteristics of elements like magnesium. Although further studies are required to characterize the extent of Mg isotope fractionation occurring during the alteration of other Mg-rich rock-forming minerals in both simple and complex systems our results indicate that variations in fluid δ^{26}Mg compositions could be used as a mechanism to help monitor CO_2 sequestration in ultramafic systems.

Associated content

Appendix 1 is thermodynamic and kinetic dataset used for the kinetic reaction path simulations.

Acknowledgements

We would like to thank Juan D. Rodriguez-Blanco and Matthijs A. Smit for help with XRD and EMPA measurements. We also thank three anonymous reviewers for constructive feedback on the original manuscript and Wolfgang Bach for editorial handling. This research was made possible by a Marie Curie grant from the European Commission in the framework of the MINSC ITN (Initial Training Research network), Project number 290040.

References

Andreani, M., Luquot, L., Gouze, P., Godard, M., Hoisé, E. and Gibert, B. (2009) Experimental study of carbon sequestration reactions controlled by the percolation of CO_2 -rich brine through peridotites. Env. Sci. Technol. **43**, 1226–1231.

Béarat, H., McKelvy, M.J., Chizmeshya, A.V.G., Gormley, D., Nunez, R., Carpenter, R.W., Squires, K. and Wolf, G.H. (2006) Carbon sequestration via aqueous olivine mineral carbonation: Role of passivating layer formation. Env. Sci. Technol. **40**, 4802–4808.

Beinlich, A., Mavromatis, V., Austrheim, H. and Oelkers, E. H. (2014) Inter-mineral Mg isotope fractionation during hydrothermal ultramafic rock alteration–Implications for the global Mg-cycle. Earth Planet Sc. Lett. **392**, 166-176.

Berndt, M.E., Allen, D.E. and Seyfried, W.E. (1996) Reduction of CO_2 during serpentinization of olivine at 300 C and 500 bar. Geology **24**, 351–354.

Brantley, S.L., and Mellott, N.P. (2000) Surface area and porosity of primary silicate minerals. Am. Mineral. **85**(11-12), 1767-1783.

Brueckner, H.K., Carswell, D.A., Griffin, W.L., Medaris, L.G., Van Roermund, H.L.M. and Cuthbert, S.J. (2010) The mantle and crustal evolution of two garnet peridotite suites from the Western Gneiss Region, Norwegian Caledonides: An isotopic investigation. Lithos **117**, 1–19.

Carroll, S., Mroczek, E., Alai, M. and Ebert, M. (1998) Amorphous silica precipitation (60 to 120°C): Comparison of laboratory and field rates. Geochim. Cosmochim. Acta **62**, 1379–1396.

Daval, D., Sissmann, O., Menguy, N., Saldi, G.D., Guyot, F., Martinez, I., Corvisier, J., Garcia, B., Machouk, I., Knauss, K.G. and Hellmann, R. (2011) Influence of amorphous silica layer formation on the dissolution rate of olivine at 90°C and elevated pCO_2. Chem. Geol. **284**, 193–209.

535 Dougan, W.K. and Wilson, A.L. (1973) Absorbtiometric determination of iron with TPTZ.
536 Water Treat. Exam. **22**, 110.
537 Etiope, G. and Sherwood Lollar, B. (2013) Abiotic methane on Earth. Rev. Geophys. **51**,
538 276-299.
539 Fishman, M. J. and Friedman, L. C. (1989) Techniques of Water Resources Investigations of
540 the United States Geological Survey. Chapter A1: Methods for determination of
541 inorganic substances in water and fluvial sediments, 3rd ed., Book 5, Laboratory
542 analysis. United States Government Printing Office.
543 Galy, A., Yoffe, O., Janney, P.E., Williams, R.W., Cloquet, C., Alard, O., Halicz, L.,
544 Wadhwa, M., Hutcheon, I.D., Ramon, E. and Carignan, J. (2003) Magnesium isotope
545 heterogeneity of the isotopic standard SRM980 and new reference materials for
546 magnesium-isotope-ratio measurements. J. Anal. At. Spectrom. **18**, 1352–1356.
547 Giammar, D.E., Bruant, R.G. and Peters, C.A. (2005) Forsterite dissolution and magnesite
548 precipitation at conditions relevant for deep saline aquifer storage and sequestration of
549 carbon dioxide. Chem. Geol. **217**, 257–276.
550 Gíslason, S.R., Wolff-Boenisch, D., Stefánsson, A., Oelkers, E.H., Gunnlaugsson, E.,
551 Sigurdardóttir, H., Sigfússon, B., Broecker, W.S., Matter, J.M. and Stute, M. (2010)
552 Mineral sequestration of carbon dioxide in basalt: A pre-injection overview of the
553 CarbFix project. Int. J. Greenh. Gas Control **4**, 537–545.
554 Gunnarsson, I., and Arnórsson, S. (2005) Precipitation of poorly crystalline antigorite under
555 hydrothermal conditions. Geochim. Cosmochim. Acta **69**, 2813-2828.
556 Gunnarsson-Robin, J., Stefánsson, A., Ono, S. and Torssander, P. (2017) Sulfur isotopes in
557 Icelandic thermal fluids. J. Volcanol. Geotherm. Res. **346**, 161-179.

Gysi, A.P. and Stefánsson, A. (2011) CO_2–water–basalt interaction. Numerical simulation of low temperature CO_2 sequestration into basalts. Geochim. Cosmochim. Acta **75**, 4728–4751.

Gysi, A.P. and Stefánsson, A. (2012a) Experiments and geochemical modeling of CO_2 sequestration during hydrothermal basalt alteration. Chem. Geol. **306-307**, 10–28.

Gysi, A.P. and Stefánsson, A. (2012b) Mineralogical aspects of CO_2 sequestration during hydrothermal basalt alteration — An experimental study at 75 to 250°C and elevated pCO_2. Chem. Geol. **306-307**, 146–159.

Hänchen, M., Prigiobbe, V., Storti, G., Seward, T. M., & Mazzotti, M. (2006). Dissolution kinetics of fosteritic olivine at 90–150 C including effects of the presence of CO_2. Geochim. Cosmochim. Acta, **70**(17), 4403-4416.

Holland, T.J.B. and Powell, R. (2011) An improved and extended internally consistent thermodynamic dataset for phases of petrological interest, involving a new equation of state for solids. J. Metamorph. Geol. **29**, 333–383.

Hövelmann, J., Austrheim, H., Beinlich, A. and Anne Munz, I. (2011) Experimental study of the carbonation of partially serpentinized and weathered peridotites. Geochim. Cosmochim. Acta 75, 6760–6779.

Huang, F., Chen, L., Wu, Z. and Wang, W. (2013) First-principles calculations of equilibrium Mg isotope fractionations between garnet, clinopyroxene, orthopyroxene, and olivine: implications for Mg isotope thermometry. Earth Planet. Sci. Lett. **367**, 61-70.

Huang, J., Li, S.G., Xiao, Y., Ke, S., Li, W.Y. and Tian, Y. (2015) Origin of low $\delta^{26}Mg$ Cenozoic basalts from South China Block and their geodynamic implications. Geochim. Cosmochim. Acta **164**, 298-317.

Huang, K-J. (2013) The behavior of magnesium isotopes during low temperature water–rock interactions. PhD dissertation. China University of Geosciences, Wuhan, China.

James, R.H., Allen, D.E. and Seyfried, W.E. (2003) An experimental study of alteration of oceanic crust and terrigenous sediments at moderate temperatures (51 to 350 °C): Insights as to chemical processes in near-shore ridge-flank hydrothermal systems. Geochim. Cosmochim. Acta **67**, 681–691.

Janecky, D.R. and Seyfried, W.E. (1986) Hydrothermal serpentinization of peridotite within the oceanic crust: Experimental investigations of mineralogy and major element chemistry. Geochim. Cosmochim. Acta **50**, 1357–1378.

Jones, L.C., Rosenbauer, R., Goldsmith, J.I. and Oze, C. (2010) Carbonate control of H_2 and CH_4 production in serpentinization systems at elevated P-Ts. Geophys. Res. Lett. **37**.

Klein, F. and Garrido, C.J. (2011) Thermodynamic constraints on mineral carbonation of serpentinized peridotite. Lithos **126**, 147–160.

King, H.E., Plümper, O. and Putnis, A. (2010) Effect of secondary phase formation on the carbonation of olivine. Env. Sci. Technol. 44, 6503–6509.

Lafay, R., Montes-Hernandez, G., Janots, E., Chiriac, R., Findling, N. and Toche, F. (2012) Mineral replacement rate of olivine by chrysotile and brucite under high alkaline conditions. J. Cryst. Growth **347**, 62–72.

Li, W., Beard, B. L., Li, C. and Johnson, C. M. (2014) Magnesium isotope fractionation between brucite [$Mg(OH)_2$] and Mg aqueous species: implications for silicate weathering and biogeochemical processes. Earth Planet. Sci. Lett **394**, 82-93.

Ling, M.X., Sedaghatpour, F., Teng, F.Z., Hays, P.D., Strauss, J. and Sun, W. (2011) Homogeneous magnesium isotopic composition of seawater: an excellent geostandard for Mg isotope analysis. Rapid Comm. Mass Spectrom. **25**, 2828-2836.

Liu, P.P., Teng, F.Z., Dick, H.J., Zhou, M.F. and Chung, S.L. (2017). Magnesium isotopic composition of the oceanic mantle and oceanic Mg cycling. Geochim. Cosmochim. Acta **206**, 151-165.

608 Lüttge, A., and Arvidson, R.S. (2008) The mineral-water interface. In Kinetics of Water-
609 Rock Interaction, edited by S.L. Brantley, J.D. Kubicki and A.F. White, 73-107,
610 Springer New York.
611 Marcaillou, C., Muñoz, M., Vidal, O., Parra, T. and Harfouche, M. (2011) Mineralogical
612 evidence for H_2 degassing during serpentinization at 300°C/300bar. Earth Planet. Sci.
613 Lett. **303**, 281–290.
614 Marieni, C., Henstock T. J. and Teagle, D.A (2013) Geological storage of CO_2 within the
615 oceanic crust by gravitational trapping. Geophys. Res. Lett. **40**, 6219-6224.
616 Mavromatis V., Harrison A.L., Eisenhauer A., Dietzel M. (2017) Strontium isotope
617 fractionation during strontianite ($SrCO_3$) dissolution, precipitation and at equilibrium.
618 Geochim. Cosmochim. Acta **218**, 201- 214.
619 Matter, J.M., Stute, M., Snæbjörnsdottir, S.Ó., Oelkers, E.H., Gislason, S.R., Aradottir, E.S.,
620 Sigfusson, B., Gunnarsson, I., Sigurdardottir, H., Gunnlaugsson, E. and Axelsson, G.
621 (2016) Rapid carbon mineralization for permanent disposal of anthropogenic carbon
622 dioxide emissions. Science **352**, 1312-1314. McCollom, T.M. and Bach, W. (2009)
623 Thermodynamic constraints on hydrogen generation during serpentinization of
624 ultramafic rocks. Geochim. Cosmochim. Acta **73**, 856–875.
625 McCollom, T.M. and Seewald, J.S. (2001) A reassessment of the potential for reduction of
626 dissolved CO_2 to hydrocarbons during serpentinization of olivine. Geochim.
627 Cosmochim. Acta **65**, 3769–3778.
628 McDonough, W.F. and Sun, S. S. (1995) The composition of the Earth. Chem. Geol. **120**,
629 223–253.
630 McGrail, B.P., Schaef, H.T., Ho, A.M., Chien, Y.-J., Dooley, J.J. and Davidson, C.L., 2006.
631 Potential for carbon dioxide sequestration in flood basalts. J. Geophys. Res. **111**.

632 Neubeck, A., Duc, N.T., Hellevang, H., Oze, C., Bastviken, D., Bacsik, Z. and Holm, N.G.
633 (2014) Olivine alteration and H_2 production in carbonate-rich, low temperature aqueous
634 environments. Planet. Space Sci. **96**, 51–61.
635 Palandri, J. L. and Kharaka, Y. K. (2004) A Compilation of Rate Parameters of Water-
636 mineral Interaction Kinetics for Application to Geochemical Modeling (No. Open-File-
637 2004-1068). Geological Survey, Menlo Park CA.
638 Palmer, D.A. and Wesolowski, D.J. (1997) Potentiometric measurements of the first
639 hydrolysis quotient of magnesium (II) to 250°C and 5 molal ionic strength (NaCl). J.
640 Solution Chem. **26**, 217–232.
641 Park, A. H. A., and Fan, L. S. (2004). CO_2 mineral sequestration: physically activated
642 dissolution of serpentine and pH swing process. Chem. Eng. Sci., **59**(22-23), 5241-
643 5247.
644 Parkhurst, D.L. and Appelo, C.A.J. (2013) Description of Input and Examples for PHREEQC
645 version 3—A computer program for speciation, batch-reaction, one-dimensional
646 transport, and inverse geochemical calculations. U.S. Geological Survey Techniques
647 and Methods, book 6, 497 pp.
648 Pearce, C. R., Saldi, G. D., Schott, J. and Oelkers, E. H. (2012) Isotopic fractionation during
649 congruent dissolution, precipitation and at equilibrium: evidence from Mg isotopes.
650 Geochim. Cosmochim. Acta **92**, 170-183.
651 Pogge von Strandmann, P.A.E., Burton, K.W., James, R.H., van Calsteren, P., Gíslason, S.R.
652 and Sigfússon, B. (2008) The influence of weathering processes on riverine magnesium
653 isotopes in a basaltic terrain. Earth Planet. Sci. Lett. **276**, 187–197.
654 Pogge von Strandmann, P.A.E., Elliott, T., Marschall, H.R., Coath, C., Lai, Y.J., Jeffcoate,
655 A.B. and Ionov, D.A. (2011) Variations of Li and Mg isotope ratios in bulk chondrites
656 and mantle xenoliths. Geochim. Cosmochim. Acta **75**, 5247–5268.

657 Pokrovsky, O.S., and Schott, J. (2000) Kinetics and mechanism of forsterite dissolution at 25
658 °C and pH from 1 to 12. Geochim. Cosmochim. Acta **64**, 3313-3325.
659 Pokrovsky, O. S., and Schott, J. (2004). Experimental study of brucite dissolution and
660 precipitation in aqueous solutions: surface speciation and chemical affinity control.
661 Geochim. Cosmochim. Acta, **68**(1), 31-45.
662 Přikryl, J., Jha, D., Stefánsson, A. and Stipp, S. L. S. (2017) Mineral dissolution in porous
663 media: An experimental and modeling study on kinetics, porosity and surface area
664 evolution. Appl. Geochem. **87**, 57-70,
665 Rimstidt, J.D., Brantley, S.L. and Olsen, A.A. (2012) Systematic review of forsterite
666 dissolution rate data. Geochim. Cosmochim. Acta **99**, 159-178.
667 Saldi, G.D., Schott, J., Pokrovsky, O.S., Gautier, Q. and Oelkers, E.H. (2012) An
668 experimental study of magnesite precipitation rates at neutral to alkaline conditions and
669 100–200°C as a function of pH, aqueous solution composition and chemical affinity.
670 Geochim. Cosmochim. Acta **83**, 93–109.
671 Saldi, G. D., Daval, D., Morvan, G., and Knauss, K. G. (2013) The role of Fe and redox
672 conditions in olivine carbonation rates: an experimental study of the rate limiting
673 reactions at 90 and 150 C in open and closed systems. Geochim. Cosmochim. Acta **118**,
674 157-183.
675 Saldi, G.D., Daval D., Guo H., Guyot F., Bernard S., Le Guillou C., Davis J.A. and Knauss
676 K.G. (2015) Mineralogical evolution of Fe–Si-rich layers at the olivine-water interface
677 during carbonation reactions. Am. Mineral. **100**, 2655-2669.
678 Seyfried, W.E., Foustoukos, D.I. and Fu, Q. (2007) Redox evolution and mass transfer during
679 serpentinization: An experimental and theoretical study at 200°C, 500bar with
680 implications for ultramafic-hosted hydrothermal systems at Mid-Ocean Ridges.
681 Geochim. Cosmochim. Acta **71**, 3872–3886.

682 Stefánsson, A. (2001) Dissolution of primary minerals of basalt in natural waters: I.
683 Calculation of mineral solubilities from 0 C to 350°C. Chem. Geol. **172**, 225–250.
684 Stefánsson, A. (2010) Low-temperature alteration of basalts–the effects of temperature, acids
685 and extent of reaction on mineralization and water chemistry. Jökull **60**, 165–184.
686 Stefánsson, A. and Barnes, J. D. (2016) Chlorine isotope geochemistry of Icelandic thermal
687 fluids: Implications for geothermal system behavior at divergent plate boundaries.
688 Earth Planet. Sci. Lett. **449**, 69-78.
689 Stefánsson, A., Bénézeth, P. and Schott, J. (2013) Carbonic acid ionization and the stability
690 of sodium bicarbonate and carbonate ion pairs to 200°C – A potentiometric and
691 spectrophotometric study. Geochim. Cosmochim. Acta **120**, 600–611.
692 Stefánsson, A., Bénézeth, P., Schott, J. (2014) Potentiometric and spectrophotometric study
693 of the stability of magnesium carbonate and bicarbonate ion pairs to 150°C and
694 aqueous inorganic carbon speciation and magnesite solubility. Geochim. Cosmochim.
695 Acta **138**, 21–31.
696 Stefánsson, A., Gunnarsson, I. and Giroud, N. (2007) New methods for the direct
697 determination of dissolved inorganic, organic and total carbon in natural waters by
698 Reagent-Free™ Ion Chromatography and inductively coupled plasma atomic emission
699 spectrometry. Anal. Chimica. Acta **582**, 69-74.
700 Stefánsson, A., Hilton, D.R., Sveinbjörnsdóttir, Á.E., Torssander, P., Heinemeier, J., Barnes,
701 J.D., Ono, S., Halldórsson, S.A., Fiebig, J. and Arnórsson, S. (2017) Isotope
702 systematics of Icelandic thermal fluids. J Volc. Geotherm. Res. **337**, 146-164.
703 Stefánsson, A., Sveinbjörnsdóttir, Á.E., Heinemeier, J., Arnórsson, S., Kjartansdóttir, R. and
704 Kristmannsdóttir, H. (2016) Mantle CO_2 degassing through the Icelandic crust:
705 Evidence from carbon isotopes in groundwater. Geochim. Cosmochim. Acta **191**, 300-
706 319.

Tang J., Dietzel M., Böhm F., Köhler S. J. and Eisenhauer A. (2008) Sr^{2+}/Ca^{2+} and $^{44}Ca/^{40}Ca$ fractionation during inorganic calcite formation: II. Ca isotopes. Geochim. Cosmochim. Acta **72**, 3733-3745.

Teng, F.Z., Li, W.Y., Rudnick, R.L. and Gardner, L.R. (2010) Contrasting lithium and magnesium isotope fractionation during continental weathering. Earth Planet. Sc. Lett. **300**, 63-71.

Teng, F.Z., Wadhwa, M. and Helz, R.T. (2007) Investigation of magnesium isotope fractionation during basalt differentiation: implications for a chondritic composition of the terrestrial mantle. Earth Planet. Sc. Lett. **261**, 84-92.

Teng, F.Z., Li, W.Y., Ke, S., Yang, W., Liu, S.A., Sedaghatpour, F., Wang, S.J., Huang, K.J., Hu, Y., Ling, M.X. and Xiao, Y. (2015) Magnesium isotopic compositions of international geological reference materials. Geostand. Geoanal. Res. **39**, 329-339.

Teng, F. Z. (2017). Magnesium isotope geochemistry. Rev. Mineral. Geochem., **82**, 219-287.

Tester, J.W., Worley, W.G., Robinson, B.A., Grigsby, C.O. and Feerer, J.L. (1994) Correlating quartz dissolution kinetics in pure water from 25 to 625°C. Geochim. Cosmochim. Acta **58**, 2407–2420.

Voigt, M., Pearce, C. R. and Oelkers, H. E. (2016) Experimental study of the Mg and Sr isotopic evolution of seawater interacting with basalt between 150 and 300 °C. Geophysical Research Abstracts 18, EGU.

Wiechert, U. and Halliday, A.N. (2007) Non-chondritic magnesium and the origins of the inner terrestrial planets. Earth Planet. Sc. Lett. **256**, 360-371.

Wimpenny, J., Colla, C. A., Yin, Q. Z., Rustad, J. R. and Casey, W. H. (2014) Investigating the behaviour of Mg isotopes during the formation of clay minerals. Geochim. Cosmochim. Acta **128**, 178-194.

731 **Figure captions**

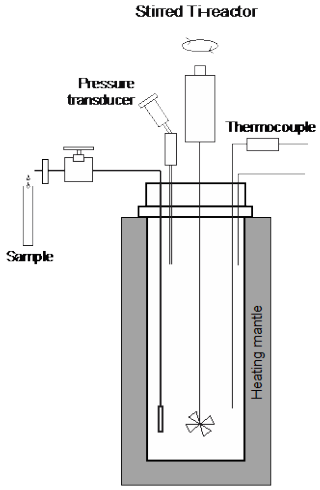

732

733 **Fig. 1.** A schematic picture of the experimental setup.

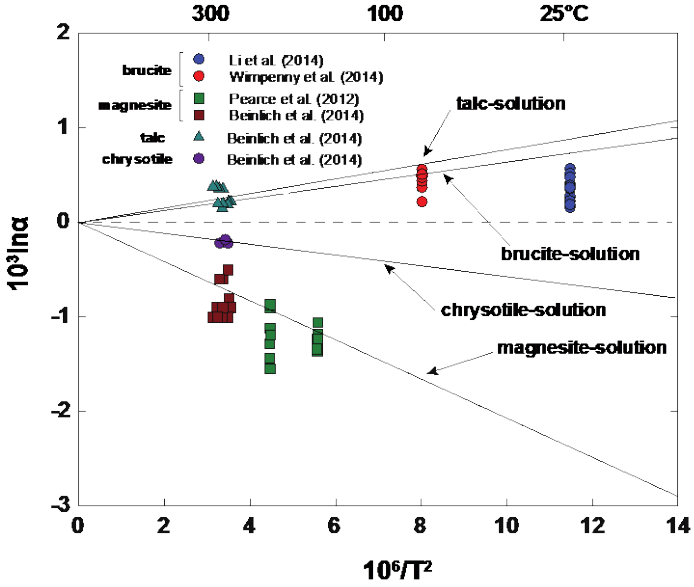

734

735 **Fig. 2.** Summary of previously reported $\delta^{26}Mg$ fractionation factors between Mg-rich
736 minerals and dissolved Mg^{2+}. The lines represent regressions through the data points
737 assuming $\alpha \rightarrow 1$ when $1/T^2 \rightarrow 0$. The data are based on results reported by Brucite from
738 Wimpenny et al. (2014), Li et al. (2014), Pearce et al. (2012) and Beinlich et al. (2014) and
739 the regression lines are consistent with the interpretations of Rustad et al. (2010) and
740 Schauble (2011).

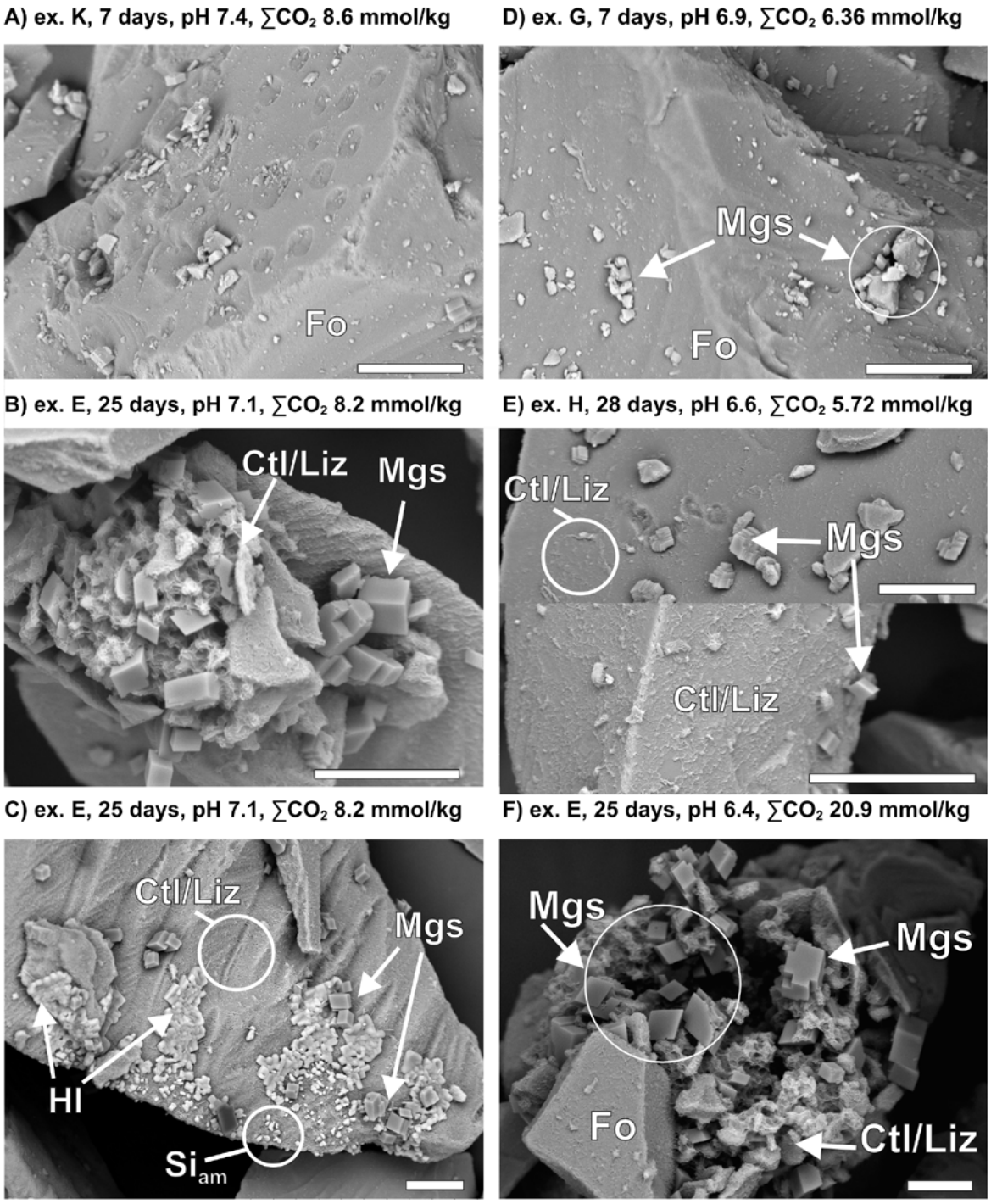

741

742 **Fig. 3.** SEM photomicrographs with typical surface of (A) reacted olivine surface showing
743 the conical or funnel-shaped etch pits, B) euhedral crystals of magnesite and conglomerates
744 of chrysotile microtubes covering Fo_{93} grains, and (C) secondary magnesite and chrysotile
745 together with spherical amorphous silica and halite flakes. Experimental conditions presented
746 are the end of the runs (A, B, C). Magnesite formation as a function of reaction time for

solutions with initially similar CO_2 concentrations (D and E), and as a function of initial low and elevated CO_2 concentrations (E and F). At low initial CO_2 concentrations of ~6 mmol/kg euhedral crystals of magnesite were observed to grow with reaction time from 1 to 5 µm in about a 3 weeks (D and E). However, the quantity and size of magnesite crystals was predominantly found to depend on initial CO_2 concentration (E and F); with elevated CO_2 concentration the magnesite grew to ~10 µm. Starting experimental pH and CO_2 conditions are presented (D, E, F). Scale bar is 15 µm on all presented SEM images, mineral abbreviations are: Ctl-chrysotile, Fo-forsterite, Hl-halite, Mgs-magnesite, Si am-amorphous silica.

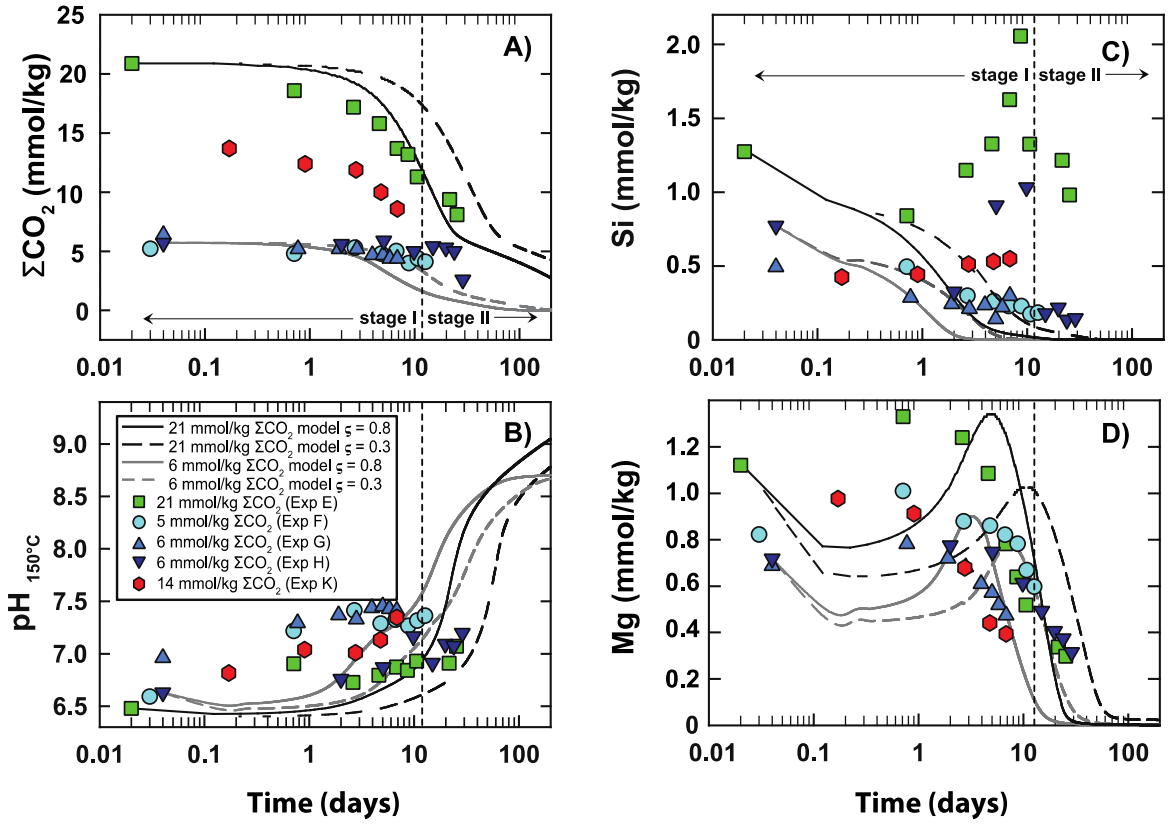

Fig. 4. Measured changes in pH, CO_2, Mg and Si concentrations in the experimental solutions as a function of time and aqueous CO_2 concentration at 150°C. The symbols denote the different CO_2 concentrations used in each experimental run, and the curved lines the results of the geochemical model. Two different models are shown, at low and elevated CO_2

761 concentrations of 6 and 21 mmol/kg, respectively, with low and high fraction of olivine
762 reactive surface areas 0.3 and 0.8 (ς). The vertical dashed line separates the two stages of
763 olivine alteration inferred by these experiments (see text for details).

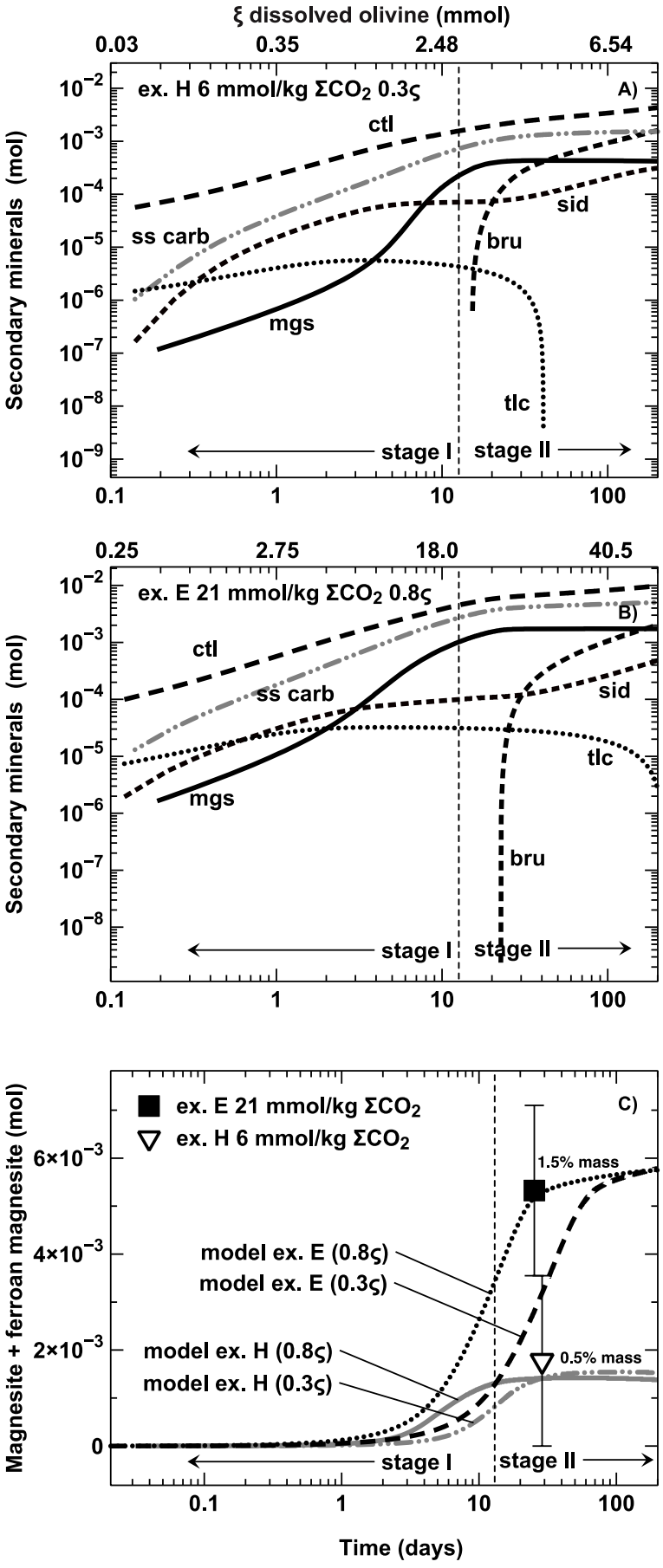
ξ dissolved olivine (mmol)
0.03
0.35
2.48
6.54
ex. H 6 mmol/kg ΣCO2 0.3ς
A)
ctl
sid
ss carb
bru
mgs
tlc
stage I
stage II
Secondary minerals (mol)
0.25
2.75
18.0
40.5
ex. E 21 mmol/kg ΣCO2 0.8ς
B)
ctl
ss carb
sid
tlc
mgs
bru
stage I
stage II
Secondary minerals (mol)
ex. E 21 mmol/kg ΣCO2
ex. H 6 mmol/kg ΣCO2
C)
1.5% mass
0.5% mass
model ex. E (0.8ς)
model ex. E (0.3ς)
model ex. H (0.8ς)
model ex. H (0.3ς)
stage I
stage II
Magnesite + ferroan magnesite (mol)
Time (days)

764

765 **Fig. 5.** Mass of secondary minerals precipitated according to the geochemical modeling for
766 low (A) and high (B) initial CO_2 concentration. Experimental magnesite mass precipitated
767 was in agreement with results from the geochemical model (C). Quantification of magnesite
768 is based on XRD analysis, SEM observations versus the geochemical model. ς is the fraction
769 of total reactive surface area applied in the model. Ctl: chrysotle; ss carb: Mg-Fe carbonate
770 solid solutions; mgs: magnesite; sid: siderite; tlc: talc; bru: brucite.

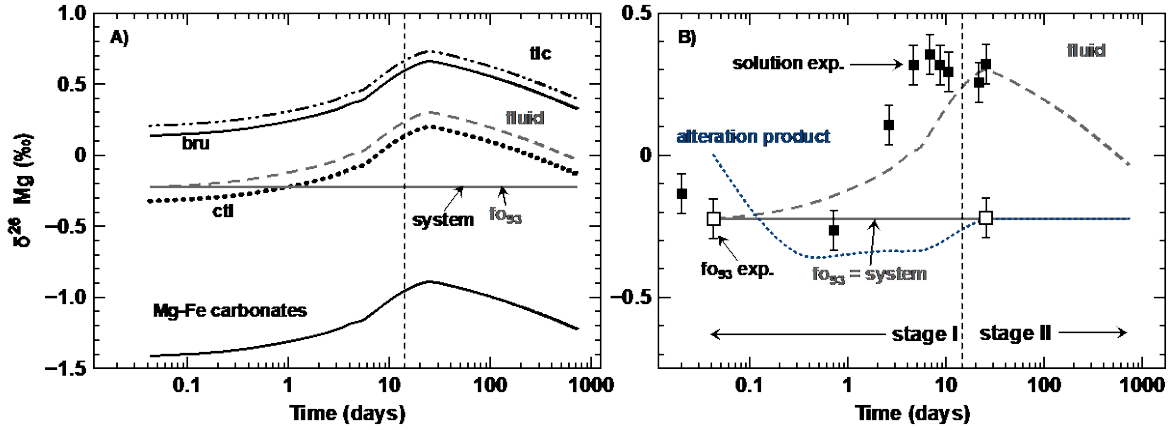

771

772 **Fig. 6.** (A) The result of the δ^{26}Mg isotopic systematics of the secondary minerals obtained
773 from the isotope modeling. (B) Comparison of the measured and calculated δ^{26}Mg isotopic
774 systematics of the water. Also shown are the δ^{26}Mg for the bulk alteration product calculated
775 using the isotope modeling results.

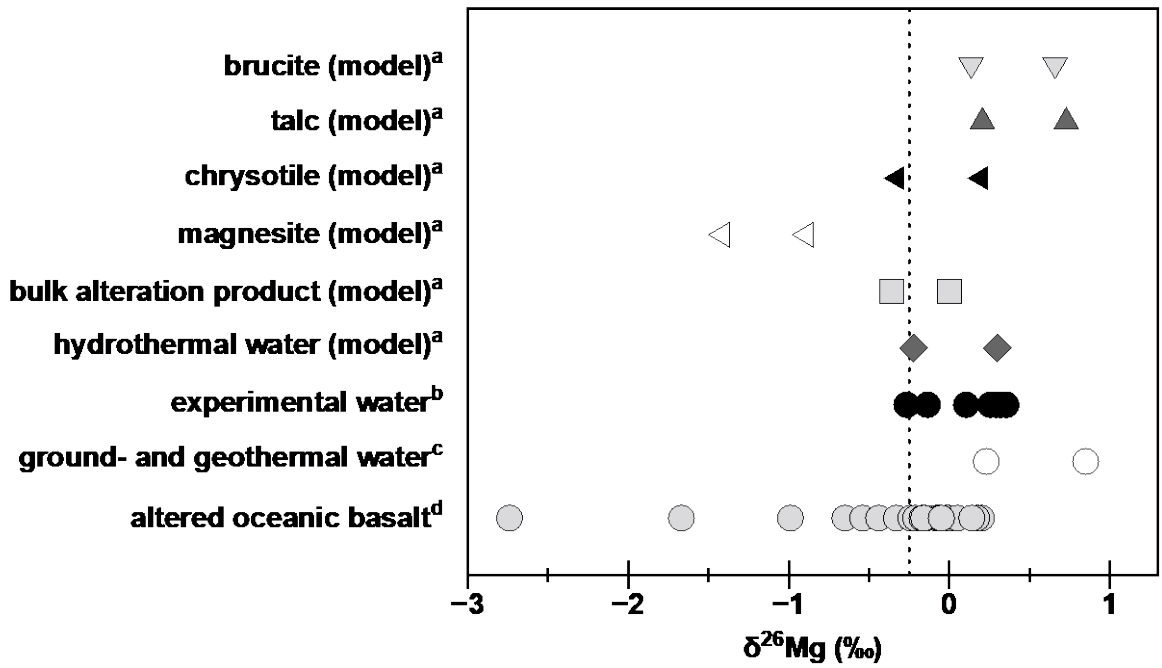

776

777 **Fig. 7.** Comparison of δ^{26}Mg ratios of natural fresh and altered mafic and ultramafic rocks,
778 natural ground- and hydrothermal water and the results obtained here experimentally and
779 using isotope modeling (min-max values): [a] this study, [b] this study, [c] Pogge von Strandmann
780 et al. (2008), [d] Huang (2013). The vertical line represents the average Mg isotopic
781 composition of the mantle (i.e., bulk Earth; Teng, 2017).

782